Enhancing Weather Radar Reflectivity Emulation from Geostationary Satellite Data Using Dynamic Residual Convolutional Network

Jianwei Si, Haonan Chen, *Senior Member, IEEE* and Lei Han, *Member, IEEE*

***Abstract*—For ground-based weather radar systems, reflectivity is particularly crucial for monitoring severe convective events. However, its limited coverage poses challenges in acquiring reliable radar data, especially for oceanic and mountainous regions. In contrast, geostationary meteorological satellites offer near-global coverage and near-real-time cloud-top observations. This paper introduces a novel deep learning-based radar reflectivity emulation method to reconstruct surface radar observations from cloud-top satellite data, termed Dynamic Residual Convolution-based Network (DRC-Net), aiming to provide more accurate and reliable reflectivity data in regions lacking radar coverage. It uniquely combines dynamic convolution, which focuses attention on convolutional kernels for dynamically adjusting weights based on input, with residual convolution, effectively enhancing network's ability to capture intricate radar echo details. Experimental results demonstrate that DRC-Net outperforms existing methods in various assessment indices, including Probability Of Detection (POD), False Alarm Ratio (FAR), Critical Success Index (CSI) and Heidke Skill Score (HSS). Generalization tests and case studies further illustrate its effectiveness in reconstructing radar reflectivity across various regions, particularly in mountainous and oceanic areas.**

***Index Terms*—Weather Radar, Dynamic Convolution, Geostationary Satellite, Reflectivity Emulation**

I. Introduction

THE ground-based weather radar can provide high-resolution and reliable data by analyzing the echo signals generated when emitted pulse waves bounce back from rain particles [1]. Reflectivity in radar observations is commonly employed to indicate the intensity of atmospheric targets, playing a crucial role in various extreme convective event monitoring missions, such as echo extrapolation and numerical weather prediction (e.g., [2]–[4]). Typically, higher reflectivity values reflect a greater likelihood of strong convective weather events, with values exceeding 35 dBZ often signifying severe convective weather [5]. However, due to radar deployment limitations such as complex terrains and high costs, most radar systems are concentrated in densely populated areas, resulting in the lack of effective radar observation data in mountainous and oceanic regions.

This research was supported by the National Natural Science Foundation of China under Grant 42275003. The work of Haonan Chen was supported by the U.S. National Science Foundation (NSF) Faculty Early Career Development Program (CAREER). (Corresponding author: Lei Han.)

Jianwei Si and Lei Han are with the Faculty of Information Science and Technology, Ocean University of China, Qingdao 266404, China (e-mails: sjw9002@stu.ouc.edu.cn; hanlei@ouc.edu.cn).

Haonan Chen is with the Department of Electrical and Computer Engineering at Colorado State University, Fort Collins, CO 80523, USA (email: haonan.chen@colostate.edu).

Unlike ground-based radars, space-based geostationary meteorological satellites primarily observe cloud-top properties, without complicated topography constraints. They can provide continuous and extensive observations at high spatial and temporal resolutions, effectively complement radar limitations and enable real-time tracking of convective events [6]–[10]. In particular, Brightness Temperature (BT) data obtained from infrared (IR) bands contain pivotal information regarding the evolution of extreme weather events. The main motivation of our work is to use cloud-top satellite observations to reconstruct surface radar reflectivity data in regions lacking radar coverage, particularly in oceanic and mountainous areas. Using these reconstructed radar reflectivity data can benefit various operational applications, such as regional or national radar mosaic products, radar extrapolation nowcasting, radar data assimilation, etc. [11].

Recently, advances in computer hardware and computational power have led to significant progress in deep learning technology. Convolutional Neural Networks (CNNs), known for their strong feature extraction capabilities, have gained substantial traction across various domains, including target tracking, image classification, object detection, as well as remote sensing [12], [13]. Several studies have explored the utilization of CNNs and BT data in retrieving radar reflectivity data. In [11], Hilburn et al. proposed a retrieval method to reconstruct radar reflectivity using lightning data and BT data from the GOES-R satellite, aiming to enhance the accuracy of short-term convective-scale predictions for high-impact weather hazards. They utilize BT and lighting data as inputs, leveraging the widely used U-Net learning model to transform these observations into radar reflectivity. Duan et al. [14] introduced a CNN-based data-driven model to reconstruct radar reflectivity in the regions without radar coverage. Four infrared channels BT data of Himawari-8 satellite are regarded as network inputs. These data are then fed into U-Net to obtain the composite reflectivity data (CREF, the maximum base reflectivity factor) of alpine areas and the ocean, which can effectively enhance predictive capability for convective storms within these areas. In [15], Wan et al. proposed a CREF retrieval model based on UNet++ and Himawari-9 satellite observations to reconstruct reflectivity data for remote offshore areas. Five infrared channel data and their differences from Himawari-9 satellite are fed into UNet++ network to obtain retrieved CREF results. Sun et al. [16] proposed to reconstruct CREF data from BT data and U-Net model. The data are from both infrared and visible channels of Fengyun-4A (FY-

4A) meteorological satellite. In [17], considering both pristine information and attention mechanism, Si et al. proposed a novel CNN-based radar reflectivity retrieval network based on feature redistribution module (FR-CNN) to retrieve CREF radar observations using FY-4A satellite data. Compared with U-Net, FR-CNN adopts a residual convolution based feature redistribution module to replace the skip connection operation, which can effectively mitigate the problem of information scarcity during network propagation. Zhao et al. [18] developed a U-Net based intelligent radar reflectivity retrieval network to reconstruct radar CREF data in beam blockage regions from FY-4A satellite observations. Two modules including hybrid convolutional module and enhanced pooling module are designed to compensate for lost spatial information and capture strong echo information. These aforementioned lightweight models utilize fixed kernel parameters after training stage, which constrains the representation ability due to static parameter assignment strategy.

A possible solution to the above limitation is dynamic convolution. Chen et al. [19] introduced the concept of dynamic convolution, an innovative approach that incorporates attention mechanisms directly into convolutional kernels. Unlike traditional convolution operations, this technique dynamically adjusts the convolutional kernel weights based on input features during network propagation, enabling CNN-based architectures to focus on critical spatial and channel-wise information, significantly enhancing their representation capacity. Inspired by dynamic convolution, Sun et al. [20] proposed Gaussian dynamic convolution, which efficiently aggregates contextual information to produce richer and more detailed features for single-image segmentation. In [21], Xiao et al. developed a dynamic convolution-based sound event detection network. The multi-dimensional frequency dynamic convolution is adopted to improve feature representation. Akbaba et al. [22] proposed a channel fusion-based dynamic convolution network for person re-identification, allowing adaptive kernel adjustments and effectively enhance feature extraction. Similarly, Soloviev et al. [23] introduced a two-branch CNN architecture leveraging dynamic convolution for image matching, achieving faster learning and superior performance compared to comparison methods. These advancements have demonstrated significant potential in improving model performance across various tasks, and their applicability will be further explored within the context of our work.

In this study, we introduce a novel radar reflectivity emulation network, Dynamic Residual Convolution based Network (DRC-Net), designed to reconstruct ground-based radar reflectivity data from FY-4A AGRI cloud-top observations. Notably, we deploy six dynamic residual convolution modules (DRMs) incorporating residual blocks and dynamic convolution blocks to capture intricate details within radar echoes. The incorporation of dynamic convolution empowers DRMs to dynamically adjust the weights of convolutional kernels based on input data, thus significantly enhancing the representation capability of DRC-Net. Furthermore, the hierarchical structure and diverse output channels in various DRMs empower DRC-Net to effectively learn complex linear and non-linear characteristics from both satellite and radar observations.

The rest of this paper is organized as follows. Section II introduces the data used in this study. Section III presents the architecture and specific details of the proposed DRC-Net. The performance evaluation of DRC-Net and other comparative methods is detailed in Section IV. Finally, Section V encapsulates the conclusions and future works of this study.

II. Data

This study utilizes Brightness Temperature (BT) data and composite reflectivity (CREF) data collected by the China Meteorological Administration (CMA). Fig. 1 presents our study domains including Fujian Province (marked as FJ) and Guizhou Province (marked as GZ). The former spans a latitude range of 23°N to 29°N and a longitude range of 115.5°E to 121.5°E, while the latter covers 24°N to 30°N and 103°E to 109°E, respectively. In this study, the data from FJ are utilized for training the proposed DRC-Net, whereas the data from GZ are used to assess its generalization ability and practical application capability.

A. Brightness Temperature Data from Fengyun-4A Satellite

The Fengyun-4A satellite is China's first new-generation meteorological satellite, equipped with three advanced optical instruments: the Advanced Geosynchronous Radiation Imager (AGRI), the Geosynchronous Interferometric Infrared Sounder and the Lightning Mapping Imager. AGRI offers a spatial resolution spanning from 0.5 km (visible channels) to 4 km (infrared channels). It can observe 14 different bands, including visible bands with central wavelengths ranging from 0.47 μm to 0.65 μm, infrared bands with central wavelengths ranging from 3.725 μm to 13.5 μm, and near-infrared bands with central wavelengths ranging from 0.825 μm to 2.225 μm. Furthermore, the satellite performs regular observations through two scanning operations: a 15-minute full disk scan and a 5-minute scan covering the Chinese continental domain.

Various AGRI channels have different central wavelengths and diverse sensitivities to cloud-top properties. In this study, inspired by [11], [24], we select the data of Band 08 (central wavelength of 3.75 μm), Band 10 (central wavelength of 6.90 μm) and Band 12 (central wavelength of 10.80 μm) of Chinese region to reconstruct radar reflectivity due to their significant correlation with cloud microphysical properties and the distribution of hydrometeors.

B. Radar Data from China New Generation Weather Radar Network

The radar data utilized in this study are sourced from the China New Generation Weather Radar Network (CINRAD) administered by the CMA. This extensive radar network encompasses more than 123 S-band and 94 C-band Doppler weather radars strategically deployed across the eastern and coastal regions, as well as the northwest and northeast areas of China [25]. The radar data adopted in this study possess a temporal resolution of 6 min and a spatial resolution of 1 km.

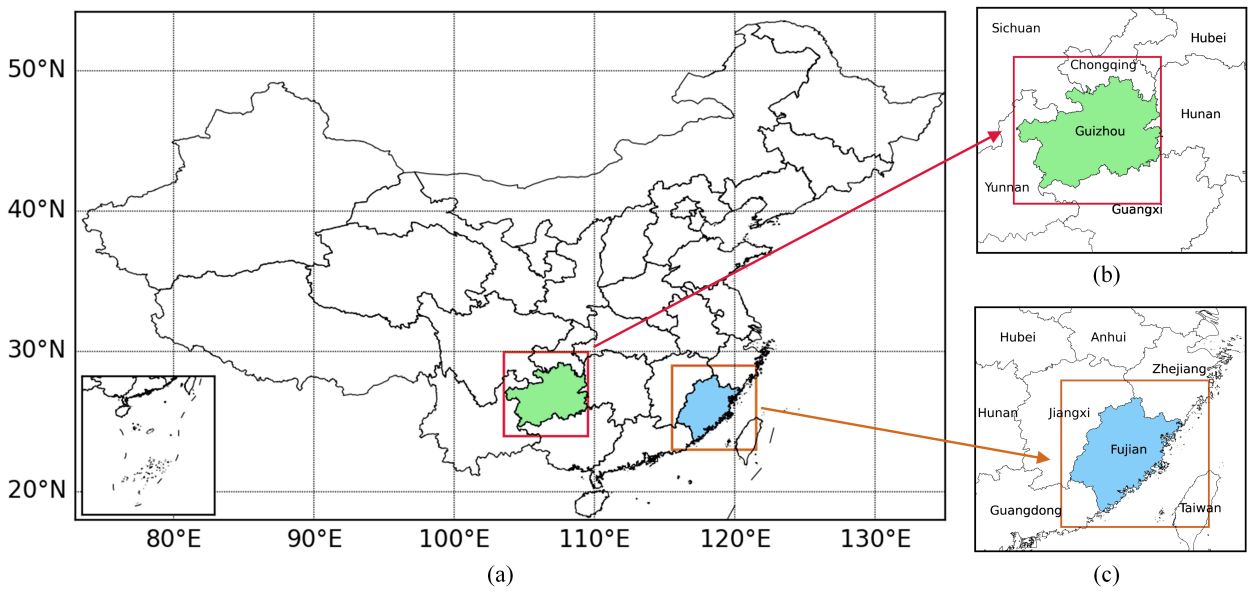

Fig. 1. Demonstration study domains. (a) map of China. (b) study domain of Guizhou Province (red rectangle). (c) study domain of Fujian Province (chocolate rectangle). Both domains are about 600 km×600 km.

C. Training Dataset Construction

In our experiments, we utilize BT data from FY-4A AGRI and CREF data from CINRAD of FJ and GZ to train and test proposed network. The data are collected during the warm seasons from May to August 2019. The satellite data have a temporal resolution of 5 min and a spatial resolution of 4 km, while the radar observations exhibit a temporal resolution of 6 min and a spatial resolution of 1 km. The size of satellite and radar data is 150×150 and 600×600 respectively. Due to the spatial resolution disparities, we employ a bilinear interpolation approach [26] to adjust satellite data to the size of 600×600. This method is chosen for its balance between computational efficiency and the preservation of spatial patterns, ensuring smooth transitions and minimizing artifacts during resampling stage. Therefore, the dimensions of multi-channel satellite and radar data input to the network are $600 \times 600 \times 3$ and 600×600 respectively. Likewise, to ensure temporal consistency, the observation time difference between satellite and radar data remains within 5 min. We select the samples with maximum radar echo more than 35 dBZ to build proposed DRC-Net.

Finally, we can obtain 17476 samples collected from May to August 2019, where 13980 samples collected from May to July for training and validation (80% of the data) and 3496 collected in August for testing (20% of the data) over the FJ area. Similarly, 3936 samples selected from May 1 to May 31 over GZ region are employed to test the generalization ability of proposed model. Then we normalize the samples for training, validation and testing processes [27].

III. Methodology

A. Overall Structure

Fig. 2 illustrates the architecture of the proposed DRMs and DRC-Net. The network primarily comprises two convolutional layers (Conv-1 and Conv-2), six DRMs (i.e. DRM-i, i=1, ...,6), and two dense layers (Dense-512 and Dense-1). The input of DRC-Net is BT data after preprocessing operation, fed into Conv-1 and Conv-2. The kernel size of the convolution layers is both set to 3×3 and the kernel number is assigned to 32 and 64 respectively. Subsequently, six DRMs, each with varying output channels, are employed to capture intricate inner structure details associated with strong echoes. Finally, two dense layers, Dense-512 and Dense-1, are utilized to generate the final CREF retrieval results based on the input BT data. Further details regarding the structure of DRMs and the proposed DRC-Net are elaborated in the following subsection.

B. Dynamic Residual Convolution Module (DRM)

Conventional light-weight models like U-Net typically assign the same static parameters to various input samples of the network after training stage, which may lead to insufficient detailed information of strong echoes and affect the representation ability and capacity. Therefore, inspired by [19], we propose six hierarchical Dynamic Residual Convolution Modules (i.e. DRM-1, DRM-2, ..., DRM-6) with residual blocks and dynamic convolution blocks to explore the inner information associated with strong radar echoes. The incorporation of dynamic convolution blocks empowers DRMs to dynamically adjust the weights of convolutional kernels based on input data. This can effectively explore inner structure information associated with strong convective events, enhancing the representation ability of DRC-Net. Moreover, inspired by [28], [29], we allocate various output channels across different DRMs and design hierarchical structure of DRC-Net to capture intricate non-linear and linear characteristics of input BT data. For DRM-1, DRM-2, and DRM-3, the number of output channels is configured as 64, 128, and 128, respectively, while that of remaining DRMs are assigned to 256.

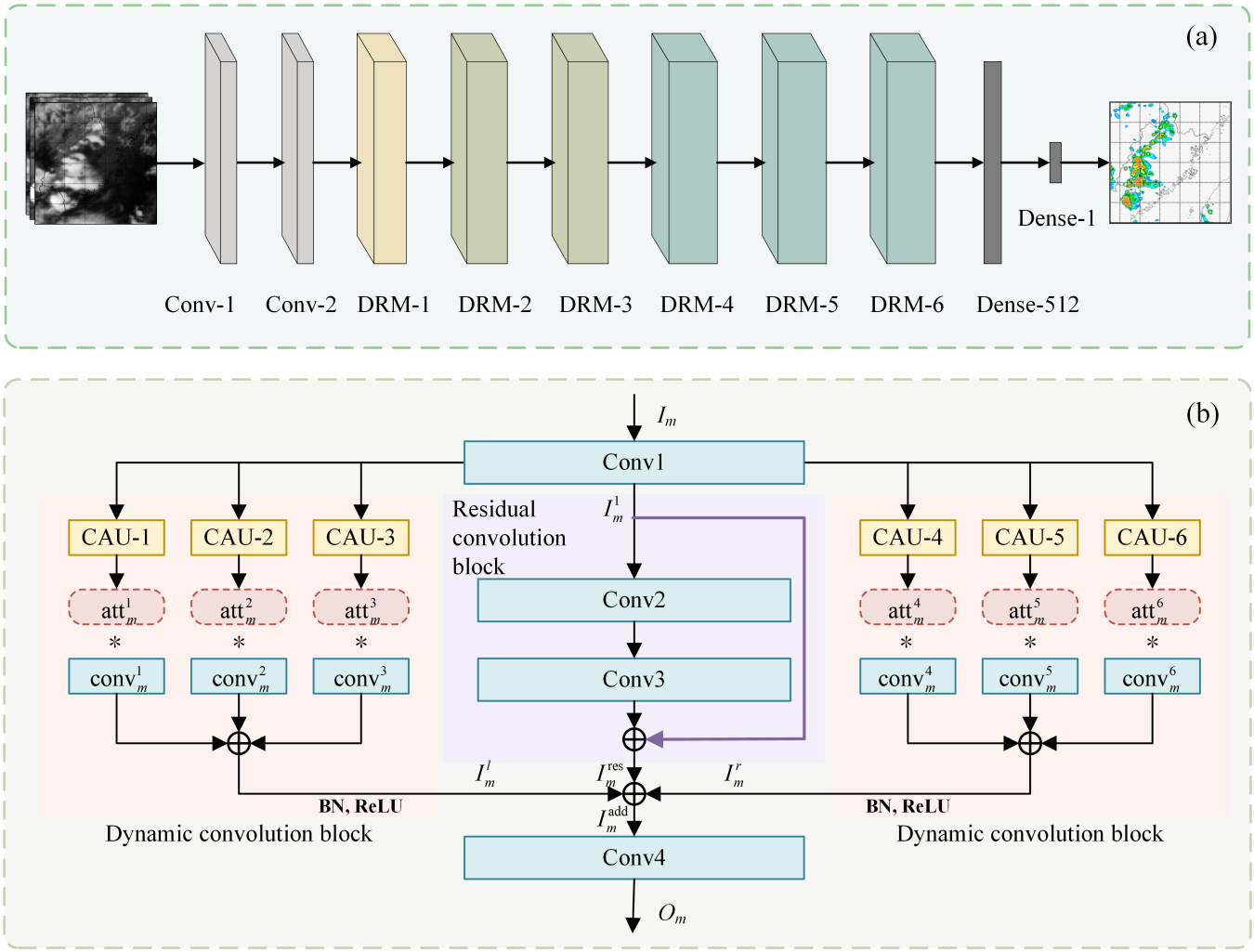

Fig. 2. Architectures of DRC-Net and DRM. (a) Architecture of the dynamic residual convolution-based network (DRC-Net). (b) Illustration of the detailed structure of Dynamic Residual convolution Module (DRM). The details of Complementary Attention Units (CAU) will be shown in Fig. 3.

Fig. 2(b) presents the architecture of each DRM, which mainly includes two convolution layers (denoted as Conv1 and Conv4), a residual block and two dynamic convolution blocks. The design of the blocks aims to extract complementary features separately and capture complex spatial patterns related to strong echoes. The input of DRMs can be represented as I_m, where m ($m \in 1, ..., 6$) represents the index of DRM. The input I_m is followed by Conv1 firstly, which is composed of a convolution operation, batch normalization and ReLU activation function [30]. The kernel number of Conv1 in DRM-1 to DRM-6 is assign to 64, 128, 128, 256, 256 and 256 respectively. The kernel size and convolution stride of the layer in DRMs are all set to 3×3 and 1 respectively. After Conv1, I_m^1 can be obtained and regarded as the input of dynamic convolution blocks and residual block.

Dynamic convolution blocks: The structure of the blocks can be found in Fig. 2(b). We take the left block as the example to introduce its structure. In the DRM, the dynamic convolution blocks are divided into two groups to achieve diversity in feature extraction while maintaining computational efficiency. The input I_m^1 is fed to several Complementary Attention Units (CAUs) (i.e. CAU-1, CAU-2 and CAU-3) to preserve key information and obtain attention weights of convolution kernels including conv_m^1, conv_m^2 and conv_m^3. Each CAU has the same structure as Fig. 3. Let I_m^1 (where $m = 1, 2, \ldots, 6$) denotes the input of the unit, which is fed into two branches firstly. One is consisted of global average-pooling, Conv-A1, ReLU and Conv-A2 operations while the other is composed of global max-pooling, Conv-M1, ReLU and Conv-M2 operations. For the convolutions, the number and kernel size of convolutional kernels are all set to 3×3 and 16 respectively. After the branches, two outputs (CA_m^t and CM_m^t, where t represents t-th CAU in m-th DRM) can be obtained. Then the outputs are fused to attain the final attention weight as follows:

$$att_m^t = \text{Softmax}(CA_m^t \times \alpha + CM_m^t \times \beta) \tag{1}$$

where α and β are the weights of branches. Considering the same importance of the branches, we set $\alpha = \beta = 0.5$. Through the CAUs including CAU-1, CAU-2 and CAU-3, the

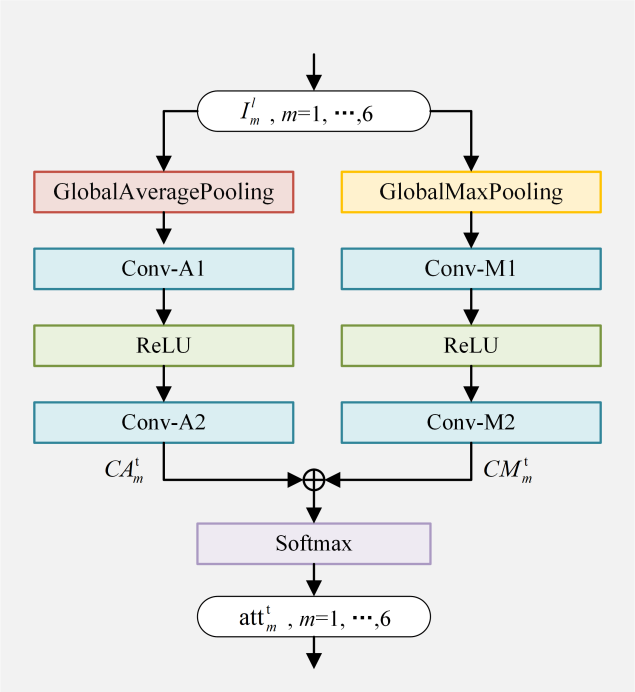

Fig. 3. The structure of Complementary Attention Units (CAU).

attention weights of conv_m^1, conv_m^2 and conv_m^3 can be acquired and represented by att_m^1, att_m^2 and att_m^3.

Then the attention weights are combined with convolution kernels to get the output of left dynamic convolution block as follows:

$$I_m^l = \text{ReLU}(\text{BN}(\sum_{j=1}^{3} att_m^j \times \text{conv}_m^j)) \tag{2}$$

where BN(·) and ReLU(·) denote batch normalization and ReLU activation function [30] respectively. Similar to left block, the input of right dynamic convolution block is I_m^l. Attention weights of convolution kernels including conv_m^4, conv_m^5 and conv_m^6 can be obtained and represented by att_m^4, att_m^5 and att_m^6. Then the weights are applied to acquire the output I_m^r as follows:

$$I_m^r = \text{ReLU}(\text{BN}(\sum_{k=4}^{6} \text{att}_m^k \times \text{conv}_m^k)) \tag{3}$$

For dynamic convolution blocks in DRMs, two outputs I_m^l and I_m^r can be obtained for subsequent operations.

Residual convolution block: The architecture of the block can also be found in Fig. 2(b). The input is I_m^1, which is fed into two convolution layers (marked as Conv2 and Conv3). In this study, the structure and kernel settings of the layers for various DRMs are fully same to Conv1. To maintain significant original information, we add the output of Conv3 and the input I_m^1 to attain the output of residual convolution block, which can be represented by I_m^{res}. The outputs of residual convolution block and dynamic convolution blocks are combined as follows:

$$I_m^{\text{add}} = I_m^l + I_m^{\text{res}} + I_m^r \tag{4}$$

Finally, I_m^{add} is filtered by Conv4 to obtain the final output of DRM, which is represented by O_m. Similar to Conv1, the kernel number of Conv4 in DRM-1 to DRM-6 is assign to 64, 128, 128, 256, 256 and 256 respectively. The kernel size and convolution stride of the layer in DRMs are all set to 3×3 and 1 respectively.

As shown in Fig. 2(a), based on the obtained fusion convolution result O_6, two dense layers Dense-512 and Dense-1 are adopted to aggregate learned high-level feature representations and map them to the final radar reflectivity emulation result, which can be symbolized as $\widehat{y}$.

IV. Experiments and Analysis

A. Training Details

We utilize TensorFlow 2.80 as the backend and implemented the network using Keras for software implementation. During the training process, the choice of a suitable loss function is crucial for achieving the expected performance. Similar to [27], a L1 loss function is employed to train DRC-Net as follows:

$$\min_\omega \frac{1}{N} \sum_{k=1}^{N} |\widehat{y}_k - y_k| \tag{5}$$

where y_k is the ground truth of the k-th input and N is the number of training patches. In addition, to expedite the convergence of proposed network, Adam optimization [31] with initial learning rate 1×10^{-4} is adopted to optimize the regression object.

B. Comparison Methods

Four experiments, U-Net, Attention U-Net (AU-Net), FR-CNN and DRC-Net, are conducted to demonstrate the performance of various networks as follows:

1) U-Net: the network is adopted in [11], equipped with conventional convolution layers, the first radar reflectivity retrieval algorithm;

2) Attention U-Net (AU-Net): the architecture is adopted in [32], considering attention mechanism in skip connections compared with U-Net;

3) FR-CNN: the structure is employed in [17], replacing skip connection with feature redistribution module to mitigate the problem of information scarcity;

4) DRC-Net: the proposed dynamic residual convolution based CREF retrieval network in this paper;

C. Evaluating Indices

The contingency table approach is employed to evaluate the emulation performance, as it is used commonly in atmospheric research. Four widely used indices, namely the Probability of Detection (POD), False Alarm Rate (FAR), Critical Success Index (CSI) and Heidke Skill Score (HSS), are employed to assess the performance of different radar reflectivity emulation

TABLE I: Definition of various index parameters.

		Observation	
		T	F
Estimation	T	TP	FP
	F	FN	TN

algorithms at various thresholds (i.e., 20, 25, 30, 35, 40 dBZ). Higher values of POD, CSI and HSS, along with lower values of FAR, indicate superior performance of the network. These indices can be calculated as follows:

$$\mathrm{POD} = \frac{\mathrm{TP}}{(\mathrm{TP} + \mathrm{FN})} \tag{6}$$

$$\mathrm{FAR} = \frac{\mathrm{FP}}{(\mathrm{FP} + \mathrm{TP})} \tag{7}$$

$$\mathrm{CSI} = \frac{\mathrm{TP}}{(\mathrm{TP} + \mathrm{FP} + \mathrm{FN})} \tag{8}$$

$$\mathrm{HSS} = \frac{2 * (\mathrm{TP} * \mathrm{TN} - \mathrm{FN} * \mathrm{FP})}{(\mathrm{FN} + \mathrm{TP}) * (\mathrm{TN} + \mathrm{FN}) + (\mathrm{TP} + \mathrm{FP}) * (\mathrm{TN} + \mathrm{FP})} \tag{9}$$

where TP, TN, FN, and FP denote true positive, true negative, false negative, and false positive, respectively. The definition of these parameters can be found in Table I, where "T" and "F" represent True and False classification results in radar reflectivity emulation restuls with the thresholds of 20, 25, 30, 35, 40 dBZ, respectively.

D. Results and Analysis

We adopt mean values of assessment indices including POD, FAR, CSI and HSS over testing dataset to quantitatively compare the performance of various methods including U-Net, AU-Net, FR-CNN and DRC-Net, which can be seen in Table II. "POD20", "FAR20", "CSI20" and "HSS20" means the POD, FAR, CSI and HSS value with the threshold of 20 dBZ, so as other thresholds including 25, 30, 35 and 40 dBZ. In the table, the best performance values are in bold. It is evident that U-Net has inferior performance across all experimental thresholds (from 20 dBZ to 40 dBZ) than other methods, exhibiting lowest POD, CSI and HSS values, and highest FAR values. AU-Net considering attention mechanism demonstrates improved performance across all thresholds in comparison to U-Net. FR-CNN achieves comparatively better performance than U-Net and AU-Net due to its consideration of both pristine information and attention mechanisms. But it has lower performance than DRC-Net due to insufficient consideration of dynamic convolution. In contrast, the proposed network with dynamic convolution-based DRMs outperforms the comparison methods at thresholds of 20 dBZ, 35 dBZ, and 40 dBZ, which can reflect the effectiveness of proposed network. It is noted that DRC-Net exhibits a higher FAR than FR-CNN at 30 dBZ (0.475 VS 0.454) and a lower HSS at 25 dBZ (0.683 VS 0.698), which may be attributed to DRC-Net's emphasis on strong echo details while potentially neglecting some comparatively low echo features. But it still has better performance than comparison metrics in other indices.

TABLE II: Performance comparison of different comparison networks.

	POD20	FAR20	CSI20	HSS20
U-Net	0.724	0.297	0.634	0.692
AU-Net	0.755	0.377	0.678	0.753
FR-CNN	0.820	0.257	0.683	0.726
DRC-Net	**0.854**	**0.252**	**0.696**	**0.767**
	POD25	FAR25	CSI25	HSS25
U-Net	0.652	0.392	0.542	0.623
AU-Net	0.714	0.320	0.570	0.657
FR-CNN	0.775	0.326	0.596	**0.683**
DRC-Net	**0.792**	**0.292**	**0.630**	0.698
	POD30	FAR30	CSI30	HSS30
U-Net	0.579	0.555	0.406	0.518
AU-Net	0.674	0.465	0.496	0.608
FR-CNN	0.723	**0.454**	0.543	0.672
DRC-Net	**0.784**	0.475	**0.592**	**0.686**
	POD35	FAR35	CSI35	HSS35
U-Net	0.331	0.583	0.258	0.368
AU-Net	0.352	0.585	0.329	0.466
FR-CNN	0.404	0.500	0.388	0.552
DRC-Net	**0.405**	**0.452**	**0.409**	**0.563**
	POD40	FAR40	CSI40	HSS40
U-Net	0.187	0.740	0.140	0.241
AU-Net	0.213	0.643	0.189	0.314
FR-CNN	0.219	0.601	0.182	0.303
DRC-Net	**0.247**	**0.558**	**0.218**	**0.353**

For qualitative comparison, Fig. 4 provides three cases of retrieved CREF data over testing dataset using U-Net, FR-CNN and proposed DRC-Net, where each line indicates a retrieval sample. U-Net exhibits poor performance by capturing fewer strong echoes compared to other methods. FR-CNN, while capturing more strong echoes than U-Net, tends to generate more false alarms in certain cases (e.g. the first sample in Fig. 4), likely due to insufficient consideration of dynamic convolution. Consequently, owing to the incorporation of the technology, DRC-Net can capture more inner structure of convective cells, signifying the effectiveness of DRMs and the proposed network. In particular, in strong echo regions, dynamic convolution blocks allow the network to adjust the importance of different convolutional kernels dynamically based on input features, which enables the model to capture subtle but critical variations in cloud-top features related to strong echoes. Furthermore, the design of two blocks for complementary feature extraction further enhances the network's ability to reconstruct intricate structures in strong echo regions.

E. Ablation Experiments

In ablation experiments, we specifically varied parameters such as the number of DRMs, the output channels of DRMs, the quantities of dynamic blocks and residual convolution blocks and mapping methods to evaluate the performance of the proposed network, without other parameters and components changed, which can be organized as follows:

1) The number of DRMs is set to 2, 4, 6 and 8 respectively, each maintaining an identical output channels of 256;

2) The output channels of DRM-1 to DRM-6, which means the number of convolution kernels in Conv4 within the blocks, are assigned to specific values:

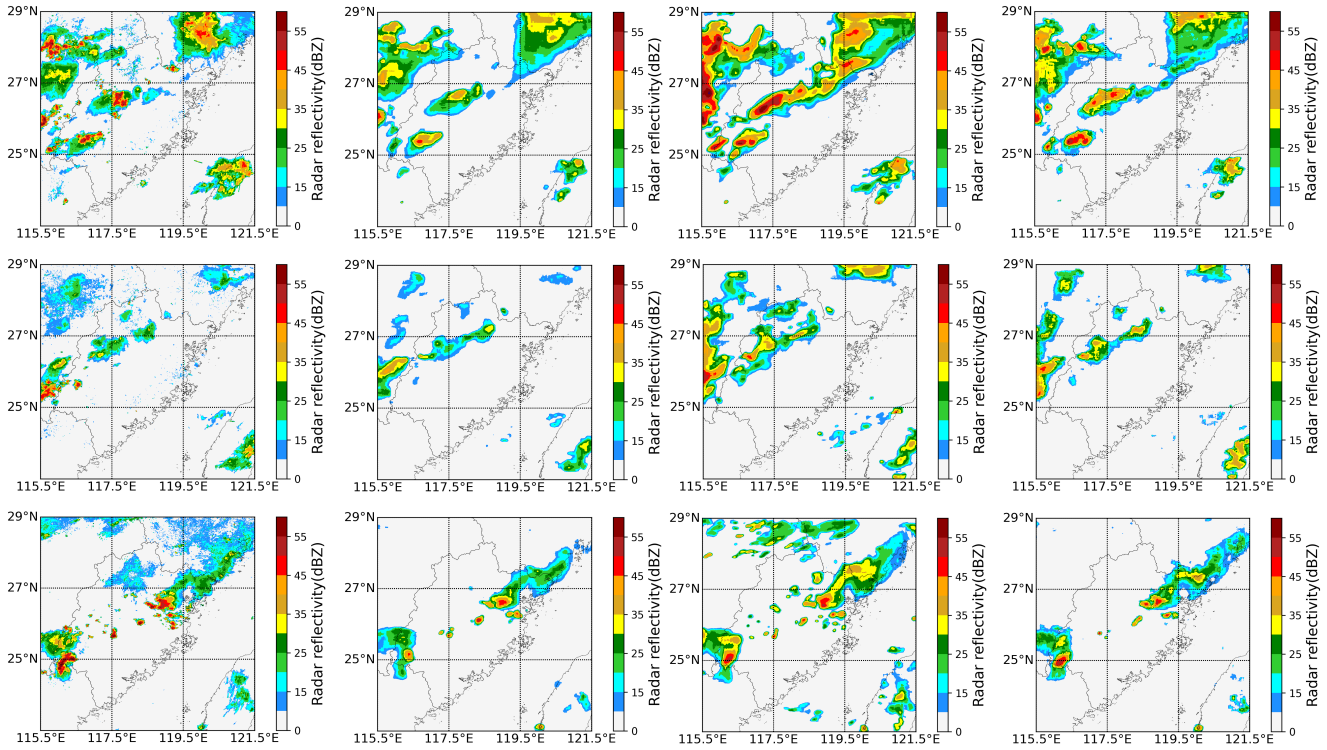

(a) Radar observation (b) U-Net (c) FR-CNN (d) DRC-Net

Fig. 4. Comparison of radar retrieval results using different networks at various times. The first row corresponds to 11:30 UTC on August 15, 2019, the second row to 14:20 UTC on August 15, 2019 and the third row to 13:50 UTC on August 29, 2019. The first column (a) displays the original radar observations, while the second (b), third (c) and fourth (d) columns present the retrieval results using U-Net, FR-CNN and DRC-Net, respectively.

TABLE III: Performance comparison with different DRM numbers at 35 dBZ threshold.

The number of DRMs	POD	FAR	CSI	HSS
2	0.302	0.643	0.357	0.421
4	0.356	0.539	0.382	0.500
6	**0.405**	**0.452**	0.409	**0.563**
8	0.403	0.482	**0.413**	0.541

TABLE IV: Performance comparison with different output channels in DRMs at 35 dBZ threshold.

Output channels in DRMs	POD	FAR	CSI	HSS
Scheme-1	0.355	0.486	0.353	0.400
Scheme-2	0.358	0.502	0.331	0.394
Scheme-3	**0.414**	**0.447**	0.392	0.489
Scheme-4	0.405	0.452	**0.409**	**0.563**

- Scheme-1: [64, 64, 64, 64, 64, 64]
- Scheme-2: [128, 128, 128, 128, 128, 128]
- Scheme-3: [64, 64, 64, 128, 128, 128]
- Scheme-4: [64, 128, 128, 256, 256, 256]

3) The number of dynamic convolution blocks is set to 0, 1, 2, 3 respectively, with 1 residual convolution block;

4) The number of residual convolution blocks is arranged to 0, 1, 2, 3 respectively, with 2 dynamic convolution blocks;

5) The mapping methods including global average pooling, point-wise convolution and dense layers are adopted to map learned high-level features to reconstructed CREF data.

TABLE V: Performance comparison with various dynamic convolution blocks in DRMs at 35 dBZ threshold.

Dynamic convolution block	POD	FAR	CSI	HSS
0	0.366	0.573	0.308	0.394
1	0.384	0.516	0.360	0.444
2	**0.405**	**0.452**	**0.409**	**0.563**
3	0.405	0.462	0.393	0.516

TABLE VI: Performance comparison with various residual convolution blocks in DRMs at 35 dBZ threshold.

Residual convolution block	POD	FAR	CSI	HSS
0	0.392	0.475	0.388	0.500
1	**0.405**	**0.452**	**0.409**	**0.563**
2	0.394	0.467	0.400	0.500
3	0.389	0.496	0.381	0.455

The experimental results of above ablation experiments are listed in Table III to Table VII respectively. It can be found that apart from CSI index in Table III, the network with 6 DRMs, 2 dynamic convolution blocks, 1 residual convolution block and dense layers achieves best performance across all experimental indices compared to other schemes. Therefore, these settings are adopted to construct the proposed DRC-Net. However, it should be noted that in Table IV, Scheme-4 exhibits a lower POD (0.405 vs 0.414) and higher FAR (0.452 vs 0.462) compared to Scheme-3. Considering a more significant improvement in CSI and HSS, Scheme-4 is chosen

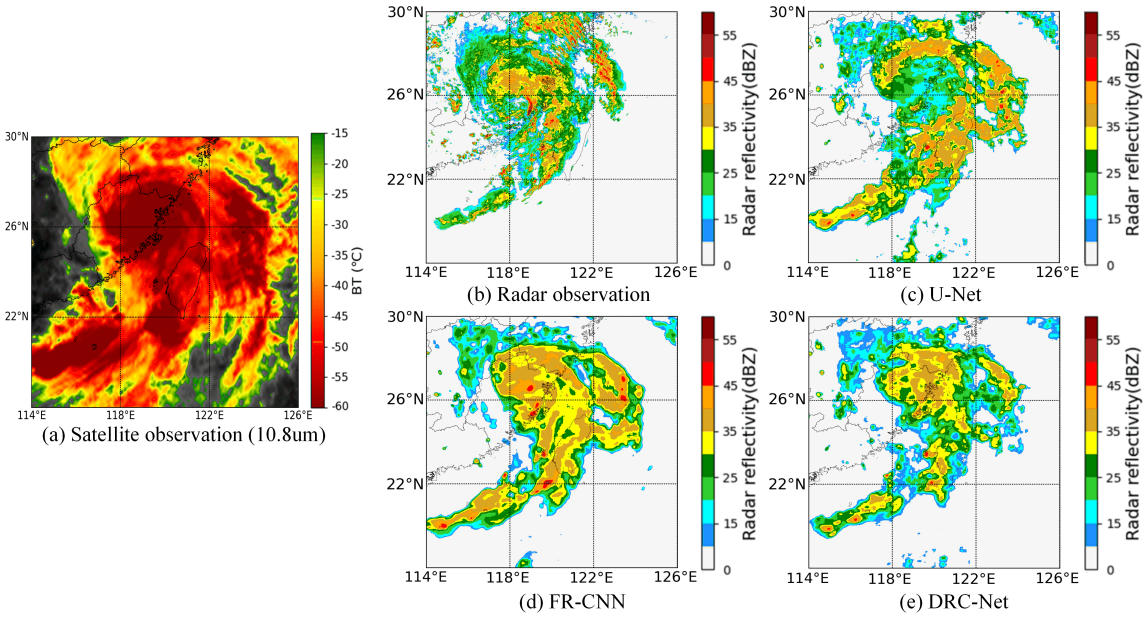

Fig. 5. Case study of typhoon Doksuri at 07:36 UTC on July 28, 2023.

TABLE VII: Performance comparison with various mapping methods at 35 dBZ threshold.

Mapping method	POD	FAR	CSI	HSS
Global average pooling	0.387	0.515	0.398	0.525
Point-wise convolution	0.391	0.477	0.400	0.542
Dense layers	**0.405**	**0.452**	**0.409**	**0.563**

to construct the proposed network.

F. Case Study of Super Typhoon Doksuri

Typhoons, characterized by their powerful winds, torrential rains, and intense storms, stand as one of the most destructive natural disasters in the world. Unless it's a landfall typhoon, ground-based radar often fails to adequately observe the typhoon. Fig. 5 shows a case study of super typhoon Doksuri at 07:36 UTC on July 28, 2023. During that period, the spiral cloud systems around the typhoon brought heavy precipitation to Philippines and Chinese eastern coastal areas. Although all methods can achieve the basic structure of the typhoon, the reflectivity obtained by the U-Net method in the eye region of the typhoon is significantly lower, which leads to a wide range of misses in the region. In contrast, FR-CNN and DRC-Net can provide comparatively better results, and our DRC-Net provides finer details of inner structure than FR-CNN and U-Net. In this case, as the typhoon is very close to land, radar can observe it completely. For typhoons that are far from land and beyond radar coverage, reconstructing surface reflectivity data using cloud-top satellite observations becomes undoubtedly valuable. This approach aids in diagnosing and forecasting the track and intensity of typhoons.

G. Generalization Performance Tests and Application

In this subsection, the generalization performance of the proposed DRC-Net can be tested by applying the trained model from the FJ area directly to generate CREF data over the GZ area. The assessment indices including POD, FAR, CSI and HSS over GZ region are adopted to quantitatively compare the performance of various networks. The comparison results are listed in Table VIII. The proposed DRC-Net demonstrates superior performance compared to other methods including U-Net, AU-Net and FR-CNN across thresholds from 20 dBZ to 40 dBZ. In terms of the the most important comprehensive metric, CSI, DRC-Net exhibited improvements ranging from 2 to 10 percentage points when compared to other methods. In all evaluations, DRC-Net only marginally lagged behind FR-

TABLE VIII: Generalization performance of various networks.

	POD20	FAR20	CSI20	HSS20
U-Net	0.759	0.336	0.560	0.680
AU-Net	0.763	0.301	0.592	0.650
FR-CNN	0.783	0.335	0.632	0.650
DRC-Net	**0.802**	**0.233**	**0.667**	**0.716**
	POD25	FAR25	CSI25	HSS25
U-Net	0.671	0.432	0.448	0.512
AU-Net	0.723	0.355	0.502	0.554
FR-CNN	0.758	0.262	0.506	0.584
DRC-Net	**0.771**	**0.230**	**0.535**	**0.637**
	POD30	FAR30	CSI30	HSS30
U-Net	0.584	0.432	0.375	0.426
AU-Net	0.616	0.459	0.403	0.486
FR-CNN	0.695	0.370	0.470	0.542
DRC-Net	**0.740**	**0.336**	**0.507**	**0.592**
	POD35	FAR35	CSI35	HSS35
U-Net	0.345	0.643	0.213	0.348
AU-Net	0.351	0.589	0.255	0.404
FR-CNN	0.341	0.531	0.331	0.497
DRC-Net	**0.383**	**0.491**	**0.415**	**0.553**
	POD40	FAR40	CSI40	HSS40
U-Net	0.152	0.794	0.133	0.245
AU-Net	0.173	0.739	0.167	0.259
FR-CNN	0.179	0.670	0.200	**0.301**
DRC-Net	**0.206**	**0.633**	**0.217**	0.299

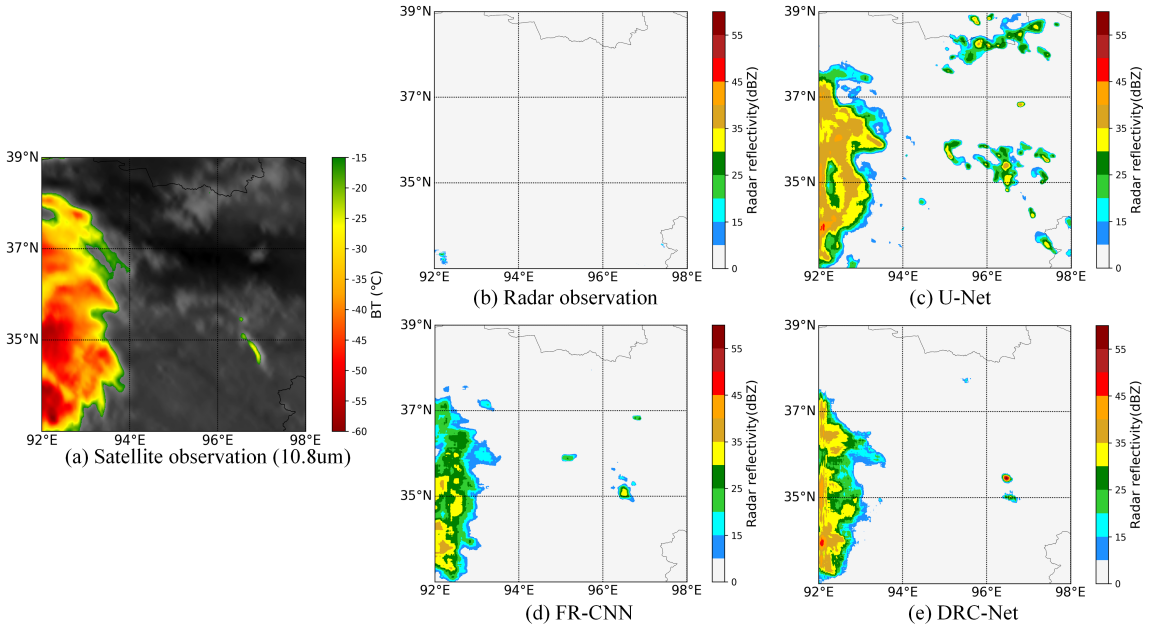

Fig. 6. A retrieved case without radar coverage at 23:20 UTC on September 19, 2023. This example illustrates the absence of radar data in the region due to insufficient deployment in mountainous areas, and demonstrates the use of satellite observations to supplement the missing information.

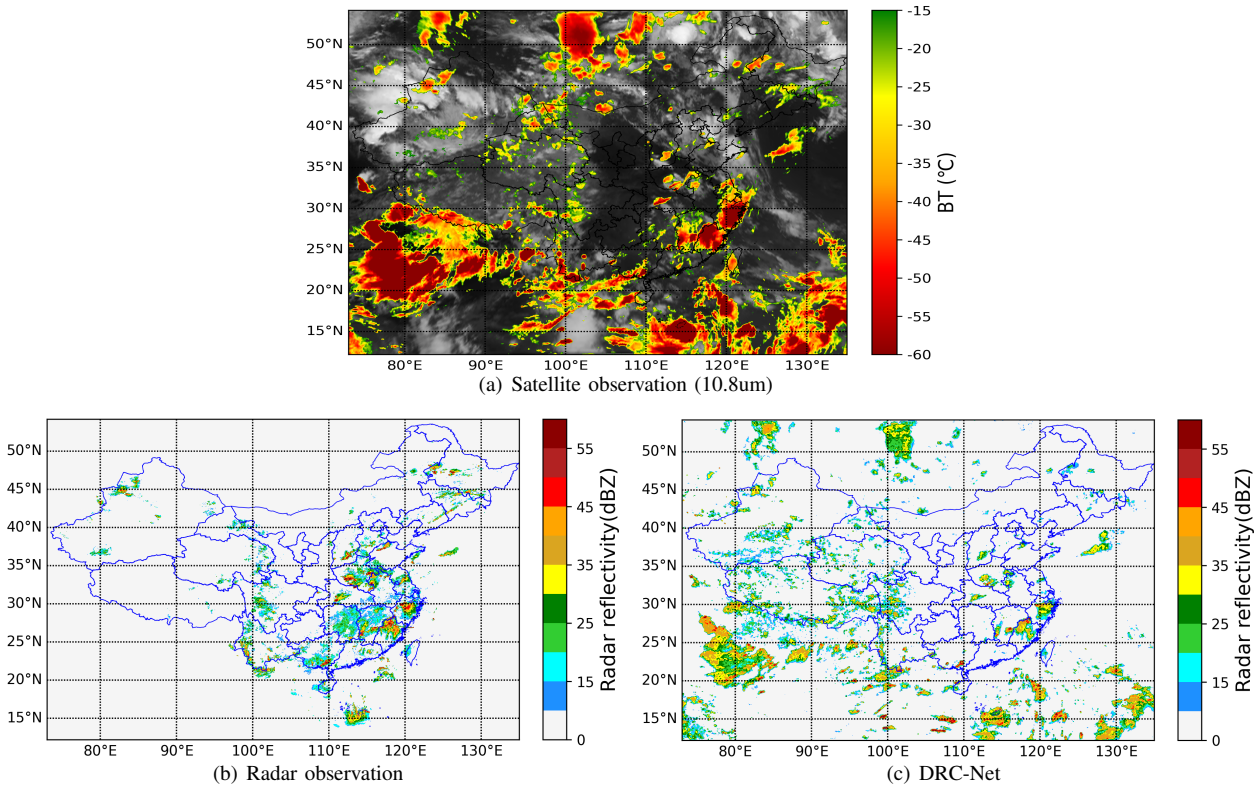

Fig. 7. A retrieved case of China region at 12:50 UTC on June 29, 2022.

CNN in the case of 40 dBZ (0.299 vs 0.310). Nevertheless, in all other assessments, DRC-Net consistently achieved superior results.

Radar data collected over the ocean and the mountainous regions plays a crucial role in monitoring and predicting destructive natural disasters. However, the availability of such data is often constrained by limitations in radar deployment. Fig. 6 presents a case of retrieved CREF data within 33°N-39°N and 92°E-98°E using U-Net, FR-CNN and proposed DRC-Net. Notably, radar echoes are absent within the region,

attributed to the lack of radar deployment, as depicted in Fig. 6(b). However, satellite observation in Fig. 6(a) reveals a large storm in this region. U-Net can capture the fundamental structure of the storm compared to satellite observation. FR-CNN, benefiting from the integration of pristine information and attention mechanisms, can retrieve comparatively more details of the storm than U-Net. In contrast, leveraging DRMs, DRC-Net can reconstruct most details of inner structure of the storm among experimental methods, surpassing U-Net and FR-CNN. Moreover, Fig. 7 presents a case of retrieved CREF data spanning the nationwide region within 12°N-54°N and 75°E-135°E using DRC-Net. It is evident that the proposed network can reconstruct radar reflectivity data in regions lacking radar coverage, particularly in oceanic and mountainous areas, leading to a better national mosaic product.

V. Conclusion

In this study, we introduce DRC-Net, a radar reflectivity emulation network designed for reconstructing surface CREF data from FY-4A satellite cloud-top observations. The key innovation lies in the design of six DRMs featuring dynamic and residual convolution blocks. Unlike conventional convolution operations, the incorporation of dynamic convolution allows for the dynamic adjustment of weights in convolutional kernels. This adaptability enables DRMs to explore more intricate structural information associated with strong radar echoes. Furthermore, the design of diverse output channels across distinct DRMs, coupled with a hierarchical structure, empowers DRC-Net to effectively capture intricate linear and non-linear features between satellite and radar observations. Experimental results underscore that the proposed DRC-Net outperforms U-Net, AU-Net and FR-CNN, showcasing superior performance in radar reflectivity reconstruction across nationwide regions, particularly in mountainous and oceanic areas. Case study highlights the network's effectiveness in retrieving inner structures of typhoon. In future works, we aim to explore advanced deep learning networks such as Generative Adversarial Networks (GANs) and Transformers to further enhance the emulation capabilities of radar reflectivity reconstruction methods.

Acknowledgments

The authors gratefully acknowledge the support of NVIDIA Corporation for the donation of the GPU used for this research. The authors would also like to thank the anonymous reviewers for providing careful reviews and comments on this article.

References

[1] H. Chen and V. Chandrasekar, "The quantitative precipitation estimation system for dallas–fort worth (dfw) urban remote sensing network," *Journal of Hydrology*, vol. 531, pp. 259–271, 2015, hydrologic Applications of Weather Radar.

[2] L. Han, Y. Zhao, H. Chen, and V. Chandrasekar, "Advancing radar nowcasting through deep transfer learning," *IEEE Transactions on Geoscience and Remote Sensing*, vol. 60, pp. 1–9, 2022.

[3] L. Han, H. Liang, H. Chen, W. Zhang, and Y. Ge, "Convective precipitation nowcasting using u-net model," *IEEE Transactions on Geoscience and Remote Sensing*, vol. 60, pp. 1–8, 2022.

[4] S. Yao, H. Chen, E. J. Thompson, and R. Cifelli, "An improved deep learning model for high-impact weather nowcasting," *IEEE Journal of Selected Topics in Applied Earth Observations and Remote Sensing*, vol. 15, pp. 7400–7413, 2022.

[5] R. D. Roberts and S. Rutledge, "Nowcasting storm initiation and growth using GOES-8 and WSR-88D data," *Weather & Forecasting*, vol. 18, no. 4, pp. 562–584, 2003.

[6] J. R. Mecikalski and K. M. Bedka, "Forecasting convective initiation by monitoring the evolution of moving cumulus in daytime GOES imagery," *Monthly Weather Review*, vol. 134, no. 1, pp. 49–78, 2006.

[7] J. R. Mecikalski, W. F. Feltz, J. J. Murray, D. B. Johnson, K. M. Bedka, S. T. Bedka, A. J. Wimmers, M. Pavolonis, T. A. Berendes, J. Haggerty *et al.*, "Aviation applications for satellite-based observations of cloud properties, convection initiation, in-flight icing, turbulence, and volcanic ash," *Bulletin of the American Meteorological Society*, vol. 88, no. 10, pp. 1589–1607, 2007.

[8] J. R. Mecikalski, K. M. Bedka, S. J. Paech, and L. A. Litten, "A statistical evaluation of GOES cloud-top properties for nowcasting convective initiation," *Monthly Weather Review*, vol. 136, no. 12, pp. 4899–4914, 2008.

[9] J. R. Walker, W. M. MacKenzie Jr, J. R. Mecikalski, and C. P. Jewett, "An enhanced geostationary satellite-based convective initiation algorithm for 0-2-h nowcasting with object tracking," *Journal of Applied Meteorology and Climatology*, vol. 51, no. 11, pp. 1931–1949, 2012.

[10] Y. Yang, H. Chen, K. A. Hilburn, R. J. Kuligowski, and R. Cifelli, "Deep learning for precipitation retrievals using ABI and GLM measurements on the GOES-R series," *IEEE Transactions on Geoscience and Remote Sensing*, vol. 61, pp. 1–14, 2023.

[11] K. A. Hilburn, I. Ebert-Uphoff, and S. D. Miller, "Development and interpretation of a Neural-Network-based synthetic radar reflectivity estimator using GOES-R satellite observations," *Journal of Applied Meteorology and Climatology*, vol. 60, no. 1, pp. 3 – 21, 2021.

[12] K. Simonyan and A. Zisserman, "Very deep convolutional networks for large-scale image recognition," in *3rd International Conference on Learning Representations (ICLR 2015)*, 2015, pp. 1–14.

[13] Y. Liu, L. Yang, M. Chen, L. Song, L. Han, and J. Xu, "A deep learning approach for forecasting thunderstorm gusts in the Beijing–Tianjin–Hebei region," *Advances in Atmospheric Sciences*, pp. 1–22, 2024.

[14] M. Duan, J. Xia, Z. Yan, L. Han, L. Zhang, H. Xia, and S. Yu, "Reconstruction of the radar reflectivity of convective storms based on deep learning and Himawari-8 observations," *Remote Sensing*, vol. 13, no. 16, p. 3330, 2021.

[15] B. Wan and C. Y. Gao, "Improving radar reflectivity reconstruction with Himawari-9 and UNet++ for off-shore weather monitoring," *Remote Sensing*, vol. 16, no. 1, 2024. [Online]. Available: https://www.mdpi.com/2072-4292/16/1/56

[16] F. Sun, B. Li, M. Min, and D. Qin, "Deep learning-based radar composite reflectivity factor estimations from Fengyun-4A geostationary satellite observations," *Remote Sensing*, vol. 13, no. 11, p. 2229, 2021.

[17] J. Si, X. Li, H. Chen, and L. Han, "A novel CNN-based radar reflectivity retrieval network using geostationary satellite observations," *IEEE Geoscience and Remote Sensing Letters*, vol. 21, pp. 1–5, 2024.

[18] J. Zhao, J. Tan, S. Chen, Q. Huang, L. Gao, Y. Li, and C. Wei, "Intelligent reconstruction of radar composite reflectivity based on satellite observations and deep learning," *Remote Sensing*, vol. 16, no. 2, 2024. [Online]. Available: https://www.mdpi.com/2072-4292/16/2/275

[19] Y. Chen, X. Dai, M. Liu, D. Chen, L. Yuan, and Z. Liu, "Dynamic convolution: Attention over convolution kernels," in *Proceedings of the IEEE/CVF conference on computer vision and pattern recognition*, 2020, pp. 11 030–11 039.

[20] X. Sun, C. Chen, X. Wang, J. Dong, H. Zhou, and S. Chen, "Gaussian dynamic convolution for efficient single-image segmentation," *IEEE Transactions on Circuits and Systems for Video Technology*, vol. 32, no. 5, pp. 2937–2948, 2021.

[21] S. Xiao, X. Zhang, P. Zhang, and Y. Yan, "Semi-supervised sound event detection with dynamic convolution and confidence-aware mean teacher," *Digital Signal Processing*, vol. 156, p. 104794, 2025.

[22] E. E. Akbaba, F. Gurkan, and B. Gunsel, "Boosting person reid feature extraction via dynamic convolution," *Pattern Analysis and Applications*, vol. 27, no. 3, p. 80, 2024.

[23] I. Soloviev, A. Kovalchuk, and V. Klinshov, "Dynamic convolution for image matching," *The European Physical Journal Special Topics*, pp. 1–9, 2024.

[24] H. Letu, T. M. Nagao, T. Y. Nakajima, J. Riedi, H. Ishimoto, A. J. Baran, H. Shang, M. Sekiguchi, and M. Kikuchi, "Ice cloud properties from Himawari-8/AHI next-generation geostationary satellite: Capability of

the AHI to monitor the DC cloud generation process," *IEEE Transactions on Geoscience and Remote Sensing*, vol. 57, no. 6, pp. 3229–3239, 2019.
[25] C. Min, S. Chen, J. J. Gourley, H. Chen, and C. Huang, "Coverage of China new generation weather radar network," *Advances in Meteorology*, vol. 2019, no. 7, pp. 1–10, 2019.
[26] H. Raveendran and D. Thomas, "Image fusion using LEP filtering and bilinear interpolation," *International Journal of Engineering Trends and Technology*, vol. 12, no. 9, pp. 427–431, 07 2014.
[27] J. Si, B. Huang, H. Yang, W. Lin, and Z. Pan, "A no-reference stereoscopic image quality assessment network based on binocular interaction and fusion mechanisms," *IEEE Transactions on Image Processing*, vol. 31, pp. 3066–3080, 2022.
[28] R. Eldan and O. Shamir, "The power of depth for feedforward neural networks," *Conference on Learning Theory*, pp. 907–940, 12 2015.
[29] Z. Lu, H. Pu, F. Wang, Z. Hu, and L. Wang, "The expressive power of neural networks: A view from the width," *Advances in neural information processing systems*, vol. 30, pp. 6231–6239, 2017.
[30] V. Nair and G. E. Hinton, "Rectified linear units improve restricted boltzmann machines," in *Proceedings of the 27th International Conference on International Conference on Machine Learning*, ser. ICML'10. Madison, WI, USA: Omnipress, 2010, p. 807–814.
[31] D. P. Kingma and J. Ba, "Adam: A method for stochastic optimization," in *3rd International Conference on Learning Representations, ICLR 2015, San Diego, CA, USA, May 7-9, 2015, Conference Track Proceedings*, Y. Bengio and Y. LeCun, Eds., 2015. [Online]. Available: http://arxiv.org/abs/1412.6980
[32] L. Yang, Q. Zhao, Y. Xue, F. Sun, J. Li, X. Zhen, and T. Lu, "Radar composite reflectivity reconstruction based on FY-4A using deep learning," *Sensors*, vol. 23, no. 1, p. 81, 2023.

Jianwei Si received the B.S. degree in safety science and engineering from Liaoning Technical University, China, in 2018, the M.S. degree in computer science and technology from Qingdao University, China, in 2021. He is currently pursuing the Ph.D. degree with the Faculty of Information Science and Engineering, Ocean University of China. His research interests include atmospheric remote sensing, radar meteorology, image processing and deep learning.

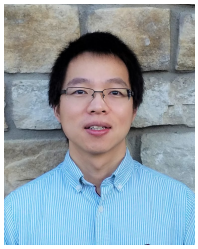

Haonan Chen (Senior Member, IEEE) received the Ph.D. degree in electrical engineering from Colorado State University (CSU), Fort Collins, CO, USA, in 2017.

He has been an Assistant Professor of Electrical and Computer Engineering, CSU, since August 2020. He is also an Affiliate Faculty with the Data Science Research Institute (DSRI), CSU. Before joining the CSU Faculty, he worked with the Cooperative Institute for Research in the Atmosphere (CIRA) and the National Oceanic and Atmospheric Administration (NOAA) Physical Sciences Laboratory, Boulder, CO, USA, from 2012 to 2020, first as a Research Student, then the National Research Council Research Associate, and a Radar, Satellite, and Precipitation Research Scientist. His research interests span a broad range of remote sensing and multidisciplinary data science, including radar and satellite remote sensing of natural disasters, polarimetric radar systems and networking, clouds and precipitation observations and processes, big data analytics, and deep learning.

Dr. Chen was a recipient of the National Science Foundation (NSF) Faculty Early Career Development Program (CAREER) Award, the Ralph E. Powe Junior Faculty Enhancement Award, the IEEE Geoscience and Remote Sensing Society (GRSS) Early Career Award, American Meteorological Society (AMS) Editor's Award, and the Office of Naval Research (ONR) Young Investigator Program (YIP) award. He served as an Associate Editor for *Journal of Atmospheric and Oceanic Technology, URSI Radio Science Bulletin*, and *IEEE Journal of Selected Topics in Applied Earth Observation and Remote Sensing*.

Lei Han (Member, IEEE) received B.Sc. degree in engineering mechanics and the M.Sc. degree in automatic control from Harbin Engineering University, Harbin, China, in 1998 and 2001; and the Ph.D. degree in in atmospheric remote sensing from Beijing University in 2008. From 2001 to 2004, he was a software engineer with Lucent R&D, Qingdao, China.

From 2013 to 2014, he was a visiting scholar with the Earth Observation Laboratory (EOL) in National Center for Atmospheric Research (NCAR), Boulder, USA. Currently, he is a Professor with the Faculty of Information Science and Engineering, Ocean University of China, Qingdao, China. His research interests include data science and AI, remote sensing of natural disasters, deep learning.